



Unbiased Differential Size Evolution and the Inside-out Growth of Galaxies in the Deep CANDELS GOODS Fields at $1 \leq z \leq 7$

A. Whitney¹ , C. J. Conselice¹ , R. Bhatwadekar¹ , and K. Duncan² ¹ University of Nottingham, School of Physics & Astronomy, Nottingham, NG7 2RD, UK² Leiden Observatory, Leiden University, P.O. Box 9513, NL-2300 RA Leiden, The Netherlands

Received 2019 March 14; revised 2019 October 17; accepted 2019 October 31; published 2019 December 16

Abstract

We present a size analysis of a sample of $\sim 49,000$ galaxies from the Cosmic Assembly Near-infrared Deep Extragalactic Survey GOODS North and South fields, using redshift-independent relative surface-brightness metrics to determine an unbiased measure of the differential size evolution of galaxies at $1 \leq z \leq 7$. We introduce a novel method of removing foreground objects from distant galaxy ($z > 3$) images that makes use of the Lyman break at 912 \AA , in what we call “2D Lyman-break imaging.” The images used are in the rest-frame optical at $z < 3$ and progressively bluer bands at $z > 3$. They are therefore subject to K-correction and cosmological dimming effects, which are tested and corrected for. We separately consider a mass-selected sample (with masses in the range $10^9 M_\odot \leq M_* \leq 10^{10.5} M_\odot$) and a number-density-selected sample (using a constant number density of $n = 1 \times 10^{-4} \text{ Mpc}^{-3}$). Instead of utilizing the commonly used, but potentially biased, effective radii for size measurements, we measure the redshift-independent Petrosian radius, defined by the parameter η , for each galaxy for three values of η , and use this as a proxy for size. The evolution of the measured radii can be described by a power law of the form $R_{\text{Petr}} = \alpha(1+z)^\beta \text{ kpc}$ where $\beta < 0$. We find that the outer radius increases more rapidly, suggesting that as a galaxy grows, mass is added to its outer regions via an inside-out growth. This growth is stronger for the number-density-selected sample, with a growth rate of nearly three in the outer radii compared to the inner. We test and confirm these results using a series of image simulations.

Unified Astronomy Thesaurus concepts: [Galaxy evolution \(594\)](#); [High-redshift galaxies \(734\)](#); [Galaxy formation \(595\)](#); [Galaxies \(573\)](#)

1. Introduction

Despite extensive research, the details of the processes that form and influence a galaxy’s evolution are still largely unknown. This will change over the next decade, with the advent of new facilities such as the *James Webb Space Telescope*. However, there is still a great deal of information to be gathered from existing data from the *Hubble Space Telescope*.

The size evolution of galaxies through redshift can tell us critical information about the potential formation scenarios undergone by the first galaxies in order to produce the galaxies seen at later times. The size of a galaxy is one of the easiest and most direct properties that can be measured. The effective radius has typically been used to determine this aspect of galaxy evolution over a range of redshifts: see, e.g., Buitrago et al. (2008), van der Wel et al. (2008), Bouwens et al. (2004), Allen et al. (2017), and Dayal & Ferrara (2018).

It has been shown, using the *HST* Advanced Camera for Surveys (ACS) and GOODS Near Infrared Camera and Multi-Object Spectrometer (NICMOS; Conselice et al. 2011a) data, that there is a strong evolution in the effective radii of galaxies since $z = 3$ (Trujillo et al. 2007; Buitrago et al. 2008; Cassata et al. 2013). This is further confirmed by the use of data from the Cosmic Assembly Near-infrared Deep Extragalactic Survey (CANDELS; Grogin et al. 2011; Koekemoer et al. 2011) and NICMOS data (Buitrago et al. 2008; van Dokkum et al. 2008; Weinzirl et al. 2011; Bruce et al. 2012; Buitrago et al. 2013; Lani et al. 2013; Patel et al. 2013; van der Wel et al. 2014). Ground-based observations also yield similar results (Carrasco et al. 2010; van Dokkum et al. 2010). These studies show a size evolution, with an increase in effective radius since $z \sim 2$ from

a factor of ~ 2 (van der Wel et al. 2008) up to a factor of ~ 7 (Buitrago et al. 2008; Carrasco et al. 2010). This strong evolution in size is consistent with simulations of massive galaxies forming through minor mergers (Naab et al. 2009; Furlong et al. 2017).

At redshifts higher than $z = 3$, a less steep evolution in size is found compared to $z < 3$, with the effective radius changing as $(1+z)^{-\beta}$ where $\beta \simeq 1$ up to $z = 7$ (Bouwens et al. 2004; Oesch et al. 2010; Straatman et al. 2015; Curtis-Lake et al. 2016; Allen et al. 2017). Probing higher up to a redshift of $z \simeq 12$, the measured sizes also fit with extrapolated data (Ono et al. 2013; Holwerda et al. 2015). Such studies, both at low and high redshifts, show that massive galaxies at $z > 1$ are significantly more compact than galaxies of a comparable mass at low redshift (Ferguson et al. 2004; Cimatti et al. 2008; Damjanov et al. 2009). Observations of galaxies at high redshifts are subject to cosmological dimming and K-correction effects, and this can lead to finding no obvious evolution in size with redshift (e.g., Law et al. 2007; Ichikawa et al. 2012; Ribeiro et al. 2016).

The cause of the observed evolution in size is thought to be a result of accretion of gas and stars from the intergalactic medium and mergers with other galaxies (e.g., Ferreras et al. 2009; López-Sanjuan et al. 2012). Conselice et al. (2013) and Ownsworth et al. (2016) show that accretion is the dominant formation mode among the most massive galaxies by calculating the evolution of stellar mass from observed star formation rates and the amount of stellar material added via mergers. Bluck et al. (2012) suggest mergers are the primary cause of the observed size evolution in massive galaxies by determining the merger history of a sample of galaxies from the GOODS NICMOS Survey. Additionally, Bluck et al. (2012)

suggest mergers can explain the majority of size evolution since $z \sim 1$, assuming mergers occur over a short timescale. Naab et al. (2009) also show this by simulating the formation of a massive spheroidal galaxy. The cosmological hydrodynamical simulation Illustris has also been used to show that the growth in size experienced by galaxies is largely caused by mergers (e.g., Wellons et al. 2016). It has also been suggested that this evolution is due to quasar feedback that removes gas from central regions, which in turn induces the expansion of the stellar distribution (Fan et al. 2008). However, the details of the processes that lead to the growth of galaxies over time are still largely unknown.

Through the study of the evolution of sizes in a sample of galaxies, we can hope to expand the understanding of the formation of galaxies. However a more refined method is now needed to make further progress on the study of galaxy sizes, and those measured using parametric fitting are often subject to biases produced by redshift. Thus, in this paper we make use of the Petrosian radius, a redshift-independent measure of the size determined by the ratio of surface brightness at a particular radius and the surface brightness within that radius (e.g., Bershady et al. 2000; Conselice 2003). It allows us to determine not only whether galaxies are growing but also where the size is growing within the galaxies, i.e., whether the inner or outer regions of a galaxy are getting larger. By using this redshift-independent measure of size in combination with a new method to remove field galaxies from images, we present in this paper an unbiased view of how galaxies are changing in size over time.

The structure of the paper is as follows: In Section 2, we describe the data and the sample used. In Section 3 we describe the methods used to remove field objects from the postage stamp images of the galaxies in our sample and to calculate the sizes of the galaxies. In Section 4, we present our results. In Section 5, we discuss our results and their implications. Finally, we present our conclusions in Section 6. Throughout this paper, we use AB magnitudes and assume a Λ CDM cosmology with $H_0 = 70 \text{ km s}^{-1} \text{ Mpc}^{-1}$, $\Omega_m = 0.3$, and $\Omega_\Lambda = 0.7$.

2. Data and Sample Selection

The data we use in this paper are taken from the ACS and the Wide Field Camera 3 (WFC3) of the (*HST*). The fields used are the GOODS North and South fields of the CANDELS (Grogin et al. 2011; Koekemoer et al. 2011). CANDELS covers a total area of 800 arcmin^2 over five different fields. GOODS North and GOODS South each cover an area of 160 arcmin^2 and are centered on the Hubble Deep Field North and the *Chandra* Deep Field South, respectively (Giavalisco et al. 2004). Both GOODS fields were part of the Deep and Wide tiers of CANDELS, which were observed using the WFC3 on *HST* (Grogin et al. 2011; Koekemoer et al. 2011), and these regions were observed in the F105W (Y_{105}), F125W (J_{125}), and F160W (H_{160}) filters. The ACS was used to observe the two fields in the F435W (B_{435}), F606W (V_{606}), F775W (i_{775}), F814W (I_{814}), and F850LP (z_{850}) filters. We use only the Deep tier, and this covers the central regions of the GOODS fields.

Our sample consists of 48,575 galaxies from both GOODS North and South fields, covering a redshift range of $1 \leq z \leq 7$ and a mass range of $10^6 M_\odot \leq M_* \leq 10^{12} M_\odot$. Details of our sample are described in Duncan et al. (2014, 2019), who make new estimates for the galaxy stellar mass function and star formation rates for this sample of galaxies in the CANDELS

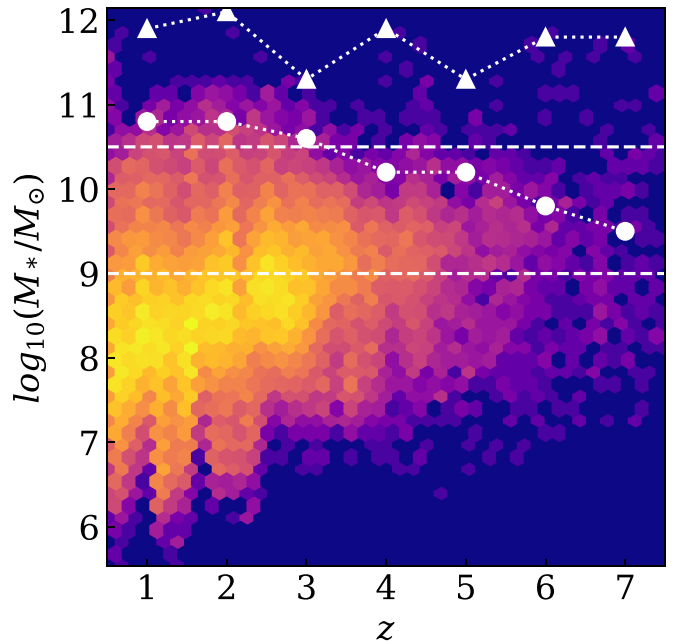


Figure 1. The galaxy stellar mass–redshift distribution for all 48,575 galaxies in our sample from the entire CANDELS area of the GOODS North and South fields; see Duncan et al. (2014, 2019) for details. The colors show the density of points, with yellow representing the highest density and dark purple representing the lowest. The completeness limits are $\log_{10}(M_*) = 8.55, 8.685, 8.85, \text{ and } 9.15$ for $z \sim 4, 5, 6, \text{ and } 7$, respectively (Duncan et al. 2014). The limits for $z < 3$ are considerably lower than our chosen lower mass limit of $10^9 M_\odot$. The mass limits for each of the samples described in 4 are shown in white; the limits of the mass-selected sample are shown as horizontal dashed lines. The upper mass limits for each of the number-density-selected samples are shown as triangles, and the lower mass limits are shown as circles.

fields. Figure 1 shows the distribution of the stellar mass and the redshift of the galaxies in our sample, with the yellow bins representing the highest density of points and the dark purple representing the lowest density. We see that the the highest concentration of mass and redshift lies at approximately $10^8 M_\odot \leq M_* \leq 10^9 M_\odot$ and $1 \leq z \leq 3$, although the sample spans all redshifts and masses. When selecting galaxies at high redshift ($z > 6$) for our sample, we visually inspect the images to remove any contaminating galaxies that are potential false-positive detections. To determine which objects were false positives, any that had no object visible in the H_{160} band image or were saturated in the H_{160} band image were removed from the sample. Figure 1 also shows the mass limits of each of the samples described in Section 4. The mass limits of the mass-selected sample are shown as horizontal dashed lines at $\log_{10}(M_*/M_\odot) = 9$ and $\log_{10}(M_*/M_\odot) = 10.5$. The upper mass limits of each redshift bin of the number-density-selected sample (constant number density of $1 \times 10^{-4} \text{ Mpc}^{-3}$) are shown as triangles, and the lower limits are shown as circles.

2.1. Photometric Redshifts

The photometric redshifts we use are calculated with the EAZY photometric redshift software (Brammer et al. 2008) by fitting all available *HST* bands to a template based on the PEGASE spectral models of Fioc & Rocca-Volmerange (1997). An additional very blue template based on a spectrum by Erb et al. (2010) is also used; it includes features expected in young galaxy populations, such as high $\text{Ly}\alpha$ equivalent widths and strong optical lines. The full redshift probability distribution

function (PDF) is constructed for each galaxy by using the χ^2 -distribution produced by EAZY. No magnitude-based prior was included in the fitting due to large uncertainties in the H -band luminosity function at higher redshifts (Henriques et al. 2012).

Where available, the calculated photometric redshifts are compared to spectroscopic redshifts, and there is a small scatter of $\sigma_{z,O} = \text{rms}(\Delta z / (1 + z_{\text{spec}})) = 0.037$ where $\Delta z = (z_{\text{spec}} - z_{\text{phot}})$. There is also a very small bias in the values, with a median value of $\Delta z = -0.04$. As such, the calculated photometric redshifts are similar to the spectroscopic redshifts from other sources.

To ensure the accuracy of the calculated photometric redshifts, the redshift for each galaxy is randomly taken from its PDF 500 times and the results are then averaged. For further details of the process, see Duncan et al. (2014) and Duncan et al. (2019).

2.2. Mass Fitting

The stellar masses used here are determined by using the custom template fitting code SMpy³ (Duncan et al. 2014) with spectral energy distributions from the synthetic stellar population models of Bruzual & Charlot (2003). Emission lines and continua are added to the templates in line with previous high-redshift fitting methods: e.g., Ono et al. (2010), Schaerer & de Barros (2010), McLure et al. (2011), Salmon et al. (2015). For full details on the mass fitting process, see Section 4 of Duncan et al. (2014).

3. Methodology

3.1. 2D Lyman-break Imaging

Here, we describe the new method we use to produce images to measure the properties of galaxies in our sample. The method uses the well-known Lyman-break drop technique where a galaxy at a certain redshift “disappears” at wavelengths redder than the Lyman limit at 912 Å, which creates a sharp break in the continuum. This break gives galaxies distinctive UV rest-frame colors, which can be used to select galaxies at specific redshifts using photometry within multiple filters. The hydrogen gas absorbs the bluest wavelengths of light, and thus the target object essentially disappears or becomes significantly fainter compared to the flux in redder bands. The break is observed at redder wavelengths as the redshift increases. For galaxies at $z = 6$ and $z = 7$, the break falls within the V_{606} band; for galaxies at $z = 5$ and $z = 4$, the break falls within the B_{435} band. The band corresponding to the break for galaxies at $z < 3$ is at a shorter wavelength than the available filters, and therefore this image processing technique is applied only to galaxies at $z \geq 4$. Note that the galaxy effectively almost disappears in filters that probe light below the Lyman limit, thus making it possible to isolate the light that belongs to these galaxies from those at lower and significantly higher redshifts. However, the majority of field objects will be at a lower redshift than the target objects, so there will be minimal contamination from those that are at higher redshifts.

The basic technique was first used by Steidel et al. (1996) to find distant galaxies as unresolved objects in ground-based imaging, but it can also be used in a two-dimensional way to remove foreground and background galaxies for systems where

the Lyman break is visible within resolved imaging, as with the *HST*. We call this “2D Lyman-break imaging,” an earlier version of which is described in Conselice & Arnold (2009).

Initially, postage stamps measuring $6'' \times 6''$ (100 pixels \times 100 pixels) in size are created from a mosaic image of the field. The postage stamps contain the target object at the center and contain other galaxies projected near the galaxy at different redshifts. In order to minimize contamination from the field objects, the target objects are isolated by removing these potentially contaminating objects. The following steps of our procedure are probably best demonstrated with images as shown in Figure 2. To remove the foreground objects, the band corresponding to the Lyman break and below is subtracted from the optical rest-frame image. The resulting image is then normalized by the optical rest-frame image. Maps of the pixels associated with the galaxy of interest are created such that the pixels corresponding to the central object are given a value of one and the pixels corresponding to the sky are given a value of zero. These are created by selecting pixels that have a value equal to or greater than three times the standard deviation of the background statistics.

This map is used in combination with the segmentation map of the optical rest-frame image to remove areas of the sky that are identified as field objects. These removed areas and objects are then replaced with noise that has the same mean and standard deviation as the sky. Figure 2 shows this process for four galaxies at redshifts of 7.0, 6.4, 4.5, and 3.7. On the left, we show the original V_{606} or B_{435} band images. Only the foreground objects are visible in these bands. In the second column, we show the optical rest-frame image for each of our sample galaxies where both the central object and potentially contaminating foreground objects are visible. In the third column, we show the corresponding segmentation map, which highlights those pixels that are associated with the target galaxy and other objects. There are small differences between the objects appearing in the blue and red images, but we always use the segmentation map that corresponds to the optical rest-frame such that these foreground objects are removed completely.

On the right of Figure 2, we show the result of the image processing where we have removed the foreground objects from the image. It is this final image in which we carry out our size analysis.

Our image processing technique can be described by the equation

$$O_{i,j}^{\text{analysis}} = \left(\frac{O_{i,j}^{\text{raw}} - D_{i,j}^{\text{raw}}}{O_{i,j}^{\text{raw}}} \cdot S_{i,j} \right) + f(O_{i,j}^{\text{raw,sky}}), \quad (1)$$

where $O_{i,j}^{\text{raw}}$ is the original optical rest-frame image or its substitute, $D_{i,j}^{\text{raw}}$ is the original drop-out image, $S_{i,j}$ is the segmentation map (shown in column 3 of Figure 2), and $f(O_{i,j}^{\text{raw,sky}})$ is some function of the raw optical rest-frame image. The function $f(O_{i,j}^{\text{raw,sky}})$ creates an image in which the pixels corresponding to the central object are zero, the pixels corresponding to the sky are those of the raw optical rest-frame image, and the pixels corresponding to the field objects are noise that has the same mean and standard deviation of the sky. Both $O_{i,j}^{\text{raw}}$ and $D_{i,j}^{\text{raw}}$ must be in the same units.

We measure the sizes of our galaxies using the images produced using our 2D Lyman-break method of removing foreground objects from the optical rest-frame images of our

³ <https://github.com/dunkenj/smpy>

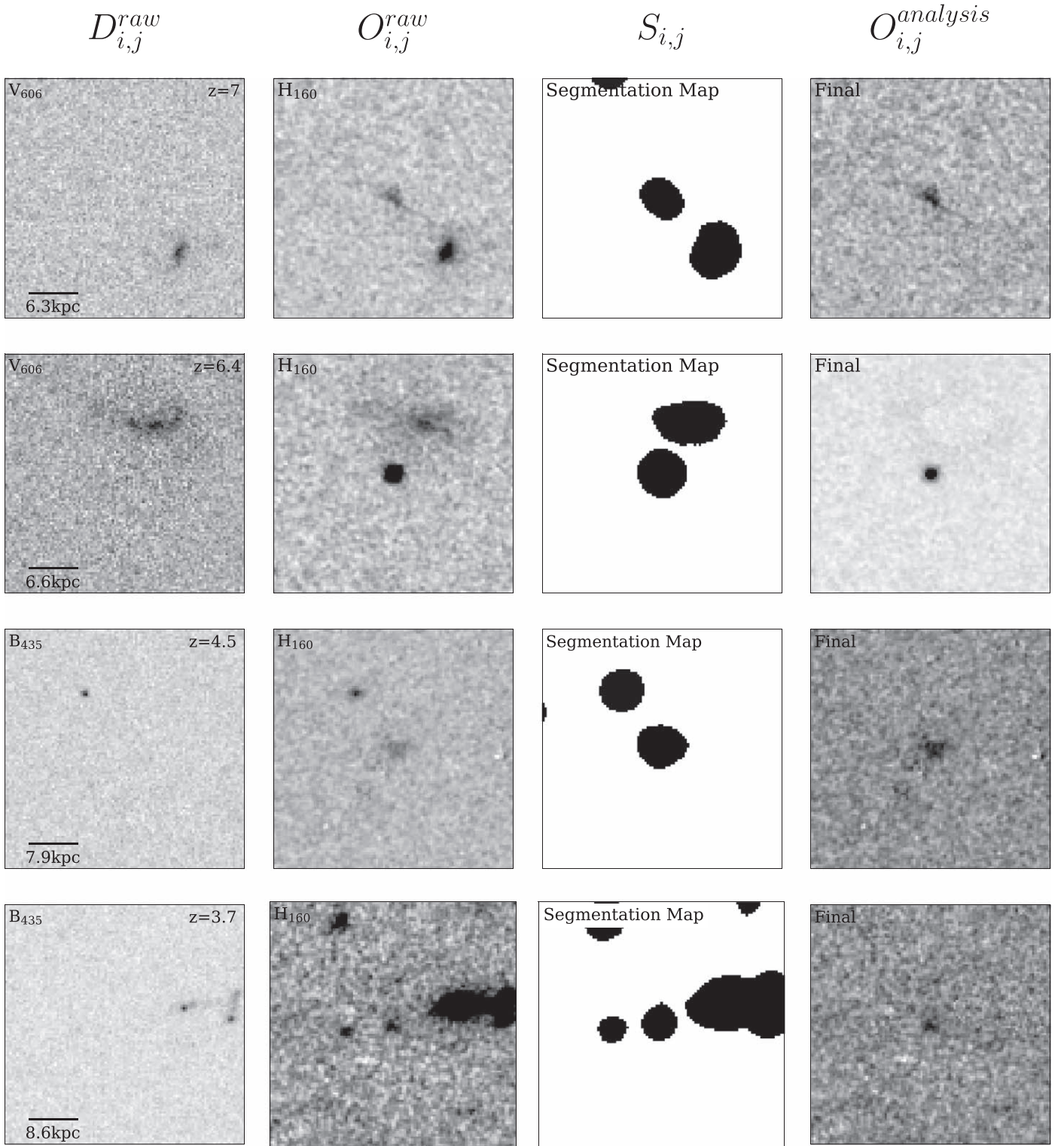


Figure 2. Examples of our image processing technique for four galaxies at redshifts of 7.0, 6.4, 4.5, and 3.7. Each column ($D_{i,j}^{raw}$, $O_{i,j}^{raw}$, $S_{i,j}$, and $O_{i,j}^{analysis}$) corresponds to the parameters of Equation (1). The first column (left) shows the original V_{606} or B_{435} image of the light below the Lyman-break rest-frame wavelength for the central galaxy’s redshift, the second column shows the original H_{160} band image, the third column shows the segmentation map corresponding to the optical rest frame, and the fourth column (right) shows the result of the image processing whereby all galaxies that appear below the Lyman break are removed (see Equation (1) for details). The field of view is $6''$ on a side.

galaxy sample. This allows us to probe the rest-frame at $\sim 4000 \text{ \AA}$ wherever possible. The bands used for the image processing are shown in Table 1, along with the rest-frame wavelength we probe at each redshift.

3.2. Galaxy Sizes

This work uses the Petrosian radius ($R_{\text{petr}}(\eta)$), which is defined as the radius at which the surface brightness at a given radius is a particular fraction of the surface brightness within

Table 1
The Bands Used to Complete the Image Processing for Each Redshift

z	$O_{i,j}^{\text{raw}}$	$D_{i,j}^{\text{raw}}$	λ_{rest}
1	I_{814}	...	4070 Å
2	J_{125}	...	4170 Å
3	H_{160}	...	4000 Å
4	H_{160}	B_{435}	3200 Å
5	H_{160}	B_{435}	2670 Å
6	H_{160}	V_{606}	2290 Å
7	H_{160}	V_{606}	2000 Å

Note. Column 1 lists the redshift. Column 2 gives the band corresponding to the optical rest frame ($O_{i,j}^{\text{raw}}$), and Column 3 gives the band corresponding to the Lyman break where applicable ($D_{i,j}^{\text{raw}}$). Column 4 gives the rest-frame wavelength probed.

that radius (e.g., Bershady et al. 2000; Conselice 2003). The concept of defining the size of a galaxy by the rate of change of light as a function of radius was first proposed by Petrosian (1976) for cosmological uses. The radius measured depends on a defined ratio ($\eta(r)$) of surface brightness. Here, $\eta(r)$ is defined as

$$\eta(r) = \frac{I(r)}{\langle I(r) \rangle}, \quad (2)$$

where $I(r)$ is the surface brightness at radius r and $\langle I(r) \rangle$ is the mean surface brightness within that radius. By this definition, $\eta(r)$ is 1 at the center and 0 at large r (Kron 1995). The Petrosian radius at $\eta = 0.2$ contains at least 99% of the light within a given galaxy (Bershady et al. 2000).

The Petrosian radius we use is determined using the CAS (concentration, asymmetry, and clumpiness) code (Conselice 2003), which provides two measurements of size (Petrosian radius and half-light radius) along with the CAS parameters. The Petrosian radius differs from the half-light radius in that the former is a redshift-independent measure of galaxy size. As such, the Petrosian radius of a particular galaxy would be, in principle, measured as the same no matter what redshift it was placed at, whereas the half-light radius would potentially decrease as the redshift increases and outer light is lost.

However, we examine this assumption and correct for the effects of the point-spread function (PSF) in the measurement of the Petrosian radii through simulating images and measuring radii in the same way as we do for our sample galaxies. In Figure 3, we show how η varies with radius r for 98 random galaxies within our sample across a range of redshifts. We show that, on average, those galaxies at the higher redshifts (yellow lines) are smaller in size than those at a given lower redshift (purple lines). The lines plotted are exponential fits of the η profiles of the form

$$\eta(r) = ae^{-cr} + d. \quad (3)$$

The horizontal lines indicate the positions of the three η values used throughout.

3.3. Simulations

To determine how well we can measure galaxy sizes through Petrosian radii, we follow the same method as Bhatwadekar et al. (2019) and simulate a sample of galaxies using the IRAF task MKOBJECTS, in order to determine how much of a correction to the measured radii is required. The sample of

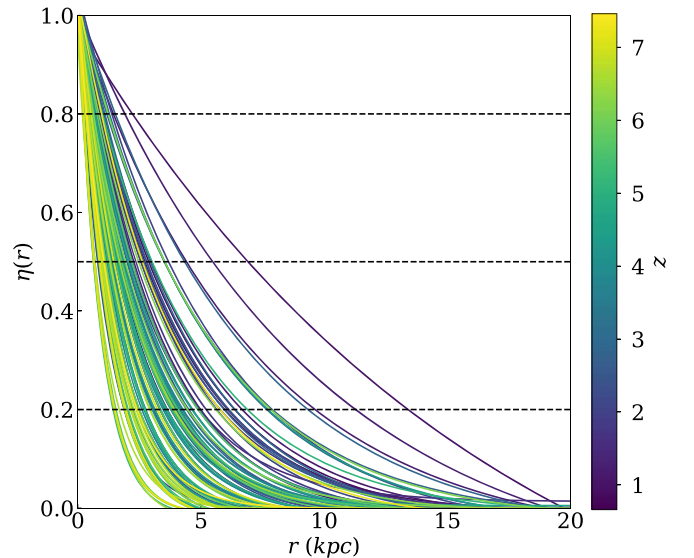


Figure 3. Exponential fits of the form $\eta(r) = ae^{-cr} + d$ of the η profiles for 98 random galaxies from our sample. These fits show that, on average, the higher-redshift galaxies are smaller than those at lower redshift. The line color corresponds to the redshift of each of the galaxies, as indicated by the color bar on the right. The three horizontal lines indicate the locations of $\eta = 0.2$, 0.5 , and 0.8 .

1912 simulated galaxies is uniformly distributed across the simulated field and a luminosity distribution in the form of a power law is applied to create a range of magnitudes. The simulated galaxies lie within a magnitude range of 21–30 and a size range of 2–42 pixels. We apply a range of surface-brightness profiles to the sample of simulated galaxies with Sérsic indices in the range $0.5 < n < 4$. The simulated galaxies are convolved using the WFC3 PSF. We use the same PSF for each of the simulated galaxies, due to the fact that any potential PSF variations do not make a significant impact at this level because we use it solely on the simulated images and not in any fits produced. After this image is created, SEXTRACTOR (Bertin & Arnouts 1996) is run on the new image to detect the sources. A postage stamp measuring 100 pixels \times 100 pixels of each object (pre- and post-convolution) is created, and examples of the simulated galaxies can be seen in Figure 4. Here, we show the images before the WFC3 PSF has been applied on the left, and the images after the PSF has been applied on the right. The CAS code we use for the real sample is then applied to this simulated sample to calculate the Petrosian radius of each of the objects in the same way as we did for our original sample. We then compare the radii measured before applying the PSF to the radii measured after the PSF is applied for each value of η (0.2, 0.5, and 0.8), and the relationship between the two is obtained through a linear fit.

The relationship between the observed and intrinsic radii for each η value for the simulated galaxies is shown in Figure 5. We show $R_{\text{Petr}}(\eta = 0.2)$ on the left, $R_{\text{Petr}}(\eta = 0.5)$ in the center, and $R_{\text{Petr}}(\eta = 0.8)$ on the right. The linear fits are shown as a red line on each of the panels. This fit is then applied to our observed sample in order to correct the measured radii. On average, all three radii change by a factor of ~ 0.8 , with the radii measured using $\eta = 0.8$ changing by $0''.036$ (0.6 pixels) on average, radii measured using $\eta = 0.5$ changing by $0''.081$ (1.35 pixels) on average, and radii measured using an $\eta = 0.2$ changing by $0''.094$ (1.56 pixels) on average. The

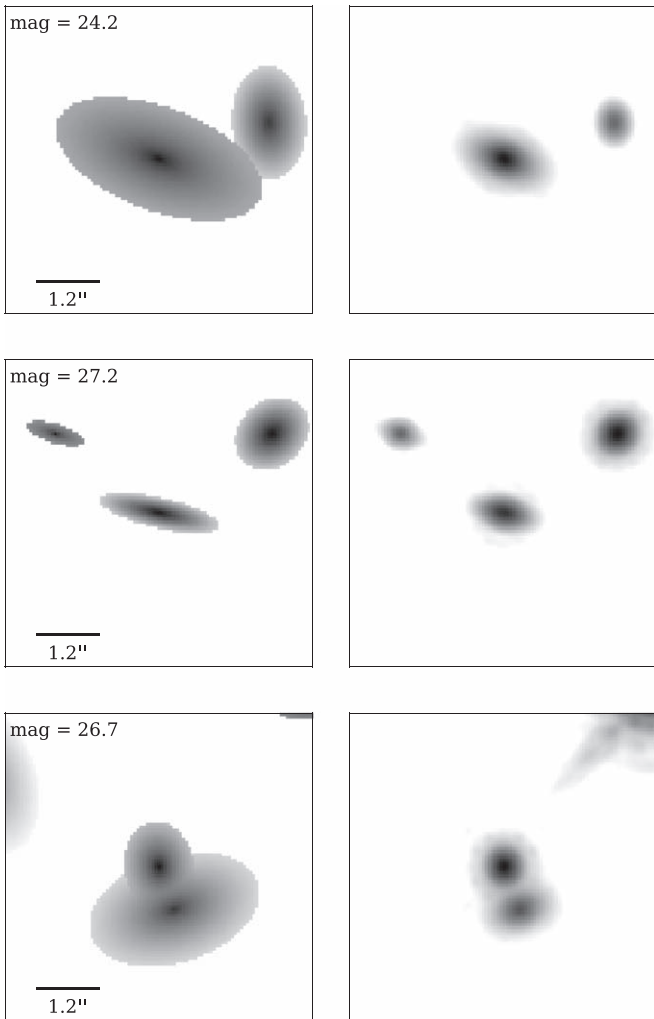


Figure 4. Examples of the simulated galaxies before (left) and after (right) the WFC3 PSF is applied. These are idealized images that we use to correct the effects of PSF on our size measurements.

change in measured size for these simulated galaxies is very small. We find the best fit between the size before and after PSF convolution using the analytical form

$$R_{\text{intrinsic}} = mR_{\text{observed}} + c. \quad (4)$$

We henceforth correct our radii using these average values.

4. Results

In this section, we present the results achieved by measuring the sizes of our galaxies in two different subsamples taken from the full sample as described in Section 2: a mass-selected sample where galaxies lie within a mass range of $10^9 M_{\odot} \leq M_{*} \leq 10^{10.5} M_{\odot}$, and a number-density-selected sample where galaxies are selected using a constant number density of $1 \times 10^{-4} \text{ Mpc}^{-3}$. Where reference is made to a galaxy’s size, this is taken to be the measured Petrosian radius.

4.1. Rest-frame Wavelength and Biases

The appearance of a galaxy depends greatly on its rest-frame wavelength, and a galaxy can have a different morphological and quantitative classification at different wavelengths (Windhorst et al. 2002; Taylor-Mager et al. 2007; Mager et al. 2018). This is

due to the fact that different wavelengths probe different aspects of a galaxy, with bluer light probing star formation and redder light probing the older existing populations of stars. The young stars can often have a distribution that is quite different from the older stars, and this needs to be accounted for if we want to measure galaxy sizes at intrinsically different rest-frame wavelengths.

This is also true of the measured surface brightness, and therefore the measured Petrosian radii. This effect is more prominent at lower redshifts when the star formation has dropped significantly. There is little star formation at low redshift. Therefore, galaxies at this epoch appear less luminous in the UV, and they consequently are often smaller in the UV than those at higher redshifts where more star formation occurs (e.g., Hopkins & Beacom 2006). Furthermore, it has been shown that, while the rest-frame UV and optical structures of galaxies are often significantly different in the local universe, this is not true at high redshifts—where galaxies are, in many ways, extremely similar in terms of structure in the rest-frame UV and optical (e.g., Papovich et al. 2003, 2005; Conselice et al. 2005, 2011b). It has also been shown that the measured size of a galaxy does not depend on the observed wavelength to the first order, even after correcting for surface-brightness dimming and PSF broadening (Ribeiro et al. 2016). Therefore, we are able to use images that correspond to the UV rest-frame at high redshifts, particularly in the case of the most massive galaxies, as the variation is not so significant for this population (Cassata et al. 2010).

Thus, we measure the sizes of galaxies in the optical rest frame at $\lambda \cong 4000 \text{ \AA}$ where possible. However, this is not possible for galaxies at $z > 3$, where we are forced to probe galaxy sizes in progressively bluer wavelengths down to the UV. To determine the bias resulting from this, we compare the sizes measured in the observed rest frame ($\lambda = 4000 \text{ \AA}$) to the intrinsic rest-frame UV at $\lambda \sim 2200 \text{ \AA}$. We do this test at the lower redshifts at $1 < z < 5$, where we have both a rest-frame optical and rest-frame UV morphology. What we find when we do this is that the sizes at both wavelengths are approximately equal. To show this, we fit a straight line of the form

$$R_{\lambda_1} = mR_{\lambda_2} + c \quad (5)$$

to the results, where R_{λ_1} is the Petrosian radius at $\eta = .02$ measured in the intrinsic bluer rest frame, and R_{λ_2} is the Petrosian radius at $\eta = 0.2$ measured in the redder rest frame. The fits for each redshift can be found in Table 2. We only include results up to $z = 5$, due to the availability of bands corresponding to the appropriate rest frame. Table 2 also gives the bands used to compare the observed and intrinsic sizes. The mean difference between these two wavelengths ($\overline{\delta R}$) is shown in Column 6 of Table 2. This difference has been normalized by the R_{λ_1} sum of the sizes measured at the two wavelengths. These values are extremely small, showing that the size measurements made at the bluer rest frame are similar in magnitude to those made at the redder rest-frame wavelength.

4.2. Redshift–Size Relation

By studying our full sample, we are able to see the effect redshift has on the size of galaxies for the full mass range. The distribution of the corrected Petrosian radii with redshift of the total sample size at three different η values can be seen in Figure 6 with $\eta = 0.2$ on the left, $\eta = 0.5$ in the middle, and

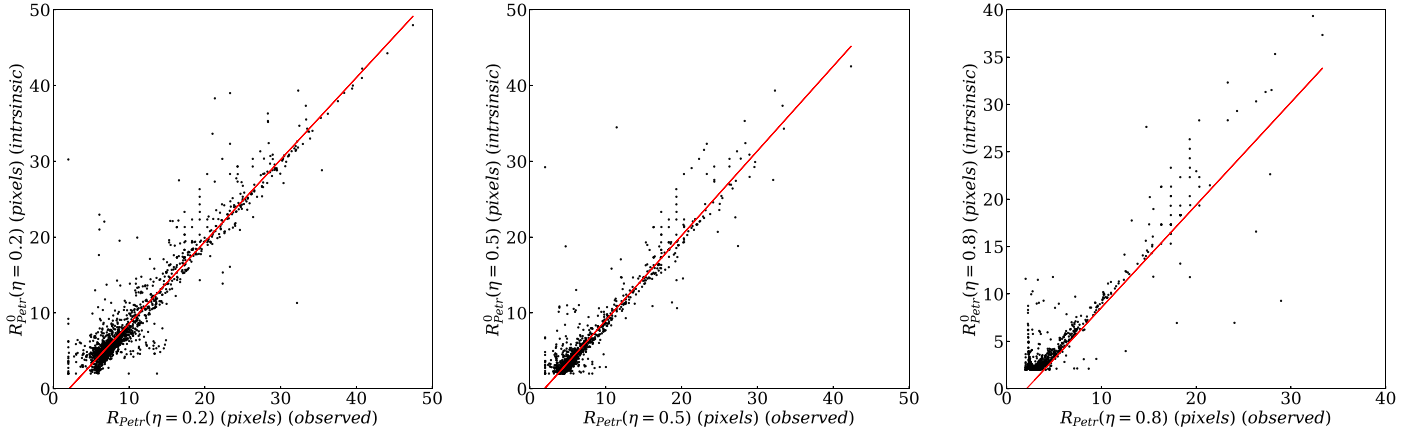


Figure 5. Relationship between the post-convolution sizes and the pre-convolution sizes measured on the simulated galaxies described in Section 3.3 for $\eta = 0.2$ (left), $\eta = 0.5$ (middle), and $\eta = 0.8$ (right). Fits of the form $R_{\text{intrinsic}} = mR_{\text{observed}} + c$ for each Petrosian radius have been plotted as a red line. For $R_{\text{Petr}}(\eta = 0.2)$, we find $m = 1.08 \pm 0.01$ and $c = -2.27 \pm 0.10$. For $R_{\text{Petr}}(\eta = 0.5)$, we find $m = 1.12 \pm 0.01$ and $c = -2.14 \pm 0.10$. For $R_{\text{Petr}}(\eta = 0.8)$, we find $m = 1.04 \pm 0.01$ and $c = -0.71 \pm 0.05$. The post-convolution sizes are, on average, changed by $0''.094$ for $\eta = 0.2$, $0''.081$ for $\eta = 0.5$, and $0''.036$ for $\eta = 0.8$.

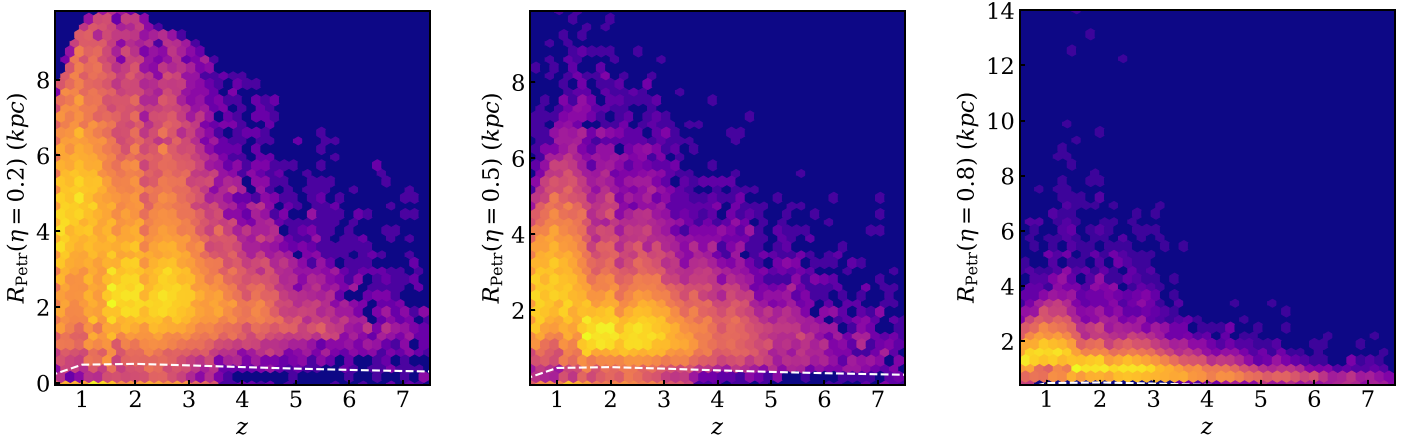


Figure 6. Galaxy size–redshift distribution for the full sample of galaxies for three different η values. Left: $\eta = 0.2$. Middle: $\eta = 0.5$. Right: $\eta = 0.8$. Yellow regions show the highest density of points, and purple the lowest. Pixel size is shown by the white dashed line.

Table 2
Observed Rest-frame Size and Intrinsic Rest-frame Size Fits

z	m	c	λ_2	λ_1	$ \frac{\delta R}{R_{\lambda_1}} $
1	0.5359 ± 0.0001	5.0641 ± 0.0053	I_{814}	B_{435}	0.06
2	0.6488 ± 0.0001	5.4437 ± 0.0044	J_{125}	V_{606}	0.63
3	0.6904 ± 0.0002	4.7803 ± 0.0156	H_{160}	z_{850}	0.41
4	0.4584 ± 0.0013	2.9556 ± 0.0635	H_{160}	Y_{105}	0.11
5	0.5941 ± 0.0015	2.3206 ± 0.0685	H_{160}	J_{125}	0.07

Note. Column 1 gives the redshift. Columns 2 and 3 give the slope and y-intercept of the fits (given by Equation (5)), including errors. Columns 4 and 5 give the bands corresponding to the observed and intrinsic rest-frame wavelengths, respectively. Column 6 gives the mean difference between the size measured in the observed and intrinsic rest-frame wavelengths. This difference has been normalized by R_{λ_1} . Here, R_{λ_1} and R_{λ_2} are the Petrosian radii measured at $\eta = 0.2$.

$\eta = 0.8$ on the right. We represent the pixel size as a white dashed line. From the definition of the Petrosian radius, $\eta = 0.2$ corresponds to a measurement made near the outer edge of a galaxy, and $\eta = 0.8$ corresponds to a measurement made in the inner regions of a galaxy. The evolution of each with redshift changes in a similar way, in that there are more

galaxies at larger radii at lower redshifts than seen at higher redshifts. However, the values of the radii differ such that the $\eta = 0.2$ values are typically much larger than those of $\eta = 0.8$, as expected.

4.3. Mass–Size Relation

From the full sample of galaxies, we are able to determine the mass–size relation as a function of redshift. In Figure 7, we show the mass–size distribution for each redshift bin. We use $R_{\text{Petr}}(\eta = 0.2)$ as a measure of size in this case. Each panel corresponds to a different redshift, showing the density of the mass–size distribution and a line of best fit. In the final panel, we show the lines of best fit for all seven redshift bins, each in the same color as their individual panels. The lines of best fit are of the form

$$\log_{10}(R_{\text{Petr}}(\eta = 0.2)) = m \log_{10}(M/M_{\odot}) + c, \quad (6)$$

and the parameters for each redshift bin are shown in Table 3. We see that the slope of the fit (m) decreases as redshift increases, showing that the sizes of the galaxies at lower redshifts have a greater dependence on their masses, compared to those galaxies at higher redshifts. We also find that the

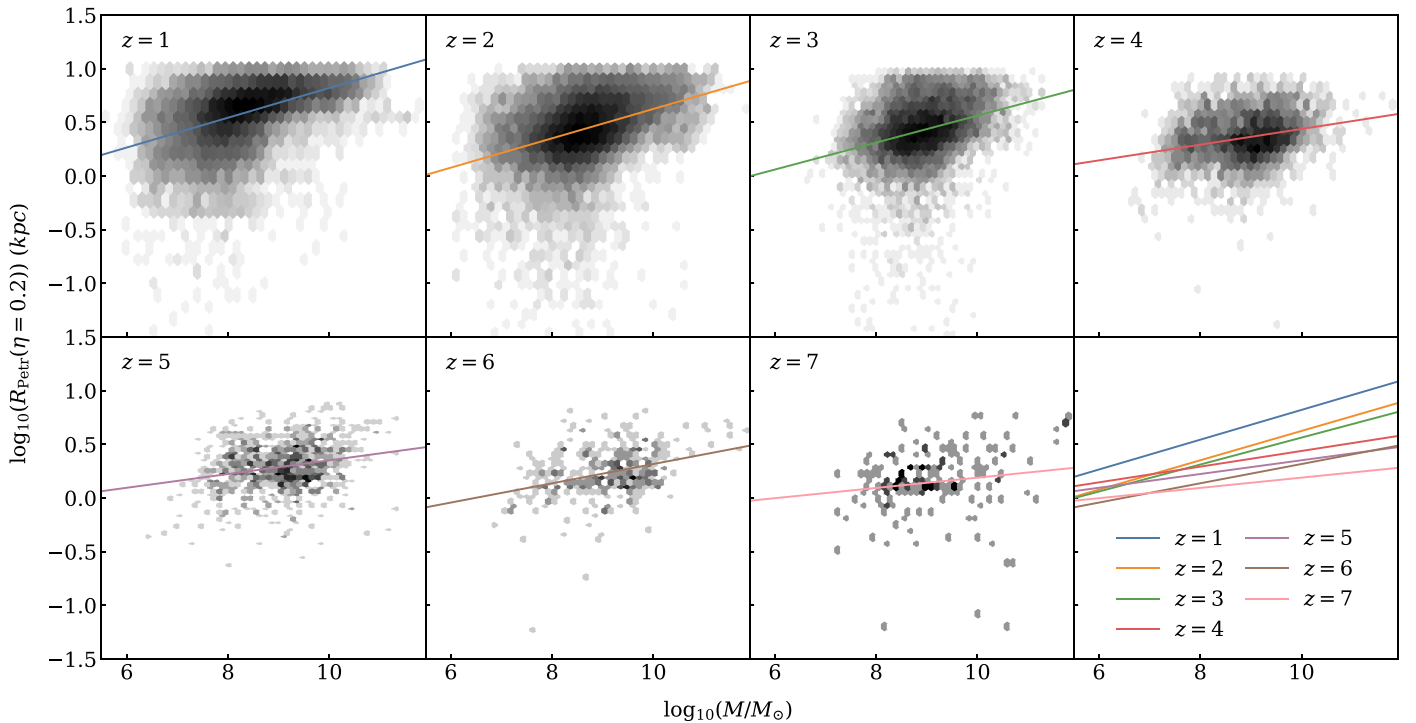


Figure 7. Galaxy stellar mass–size distributions for the full sample of galaxies. The size measurement is given by $R_{\text{Petr}}(\eta = 0.2)$. Each panel shows the distribution of a different redshift along with a line of best fit given in Equation (6). In the final panel, we show the fitted mass–size relation for each redshift, using the same colored lines as in the individual panels. The gradient of each best fit is positive, but it decreases as redshift increases. The best-fit parameters are given in Table 3.

intercept (c), on average, decreases as z increases, showing an evolution in size.

4.4. Mass-selected Sample

Here, we present the results of the analysis of a mass-selected sample ($10^9 M_\odot \leq M_* \leq 10^{10.5} M_\odot$) of 14,015 galaxies taken from the full sample. This mass range is chosen for completeness (Duncan et al. 2014). A mass-selected sample allows us to remove biases present in the full sample due to the detection limits of the surveys.

Comparing the median sizes of the galaxies in our sample at different epochs shows how the sizes evolve with redshift. Figure 8 shows the evolution of the median corrected radii of our mass-selected sample. The blue circles show the evolution of the $R_{\text{Petr}}(\eta = 0.2)$ values, the orange diamonds show the evolution of $R_{\text{Petr}}(\eta = 0.5)$, and the green squares show the evolution of $R_{\text{Petr}}(\eta = 0.8)$. There is a clear change in each of the radii measurements from $z = 7$ to $z = 1$, particularly in the case of $\eta = 0.2$. We find that $R_{\text{Petr}}(\eta = 0.2)$ increases by a factor of 3.78 ± 0.39 from $z = 7$ to $z = 1$, whereas $R_{\text{Petr}}(\eta = 0.8)$ increases by a factor of 3.20 ± 0.19 . We fit a simple power-law relation to the median measured sizes for each η value of the form

$$R_{\text{Petr}}(\eta) = \alpha(1 + z)^\beta \text{kpc}. \quad (7)$$

The values we find for α and β for each of the methods and η values can be seen in Table 4. The values for α and β for the mass-selected sample can be seen in columns 2 and 3. In Figure 8, the power-law fits for the full samples are shown as a blue dotted line for $R_{\text{Petr}}(\eta = 0.2)$, an orange dashed line for $R_{\text{Petr}}(\eta = 0.5)$, and a green solid line for $R_{\text{Petr}}(\eta = 0.8)$.

Table 3
Parameters Determined for the Mass–Size Relation (Shown in Figure 7)

z	m	c
1	0.15 ± 0.00	-0.75 ± 0.00
2	0.14 ± 0.00	-0.70 ± 0.00
3	0.14 ± 0.00	-0.75 ± 0.00
4	0.07 ± 0.00	-0.28 ± 0.00
5	0.06 ± 0.00	-0.25 ± 0.01
6	0.09 ± 0.00	-0.55 ± 0.02
7	0.05 ± 0.00	-0.29 ± 0.07

Note. The fits are given in the form $\log_{10}(R_{\text{Petr}}(\eta = 0.2)) = m \log_{10}(M/M_\odot) + c$. Where the error is given as 0.00, it is negligible in comparison to the value of the parameter.

4.5. Number-density-selected Sample

Instead of selecting a sample of galaxies by their mass, in this selection we create a sample of galaxies based on a constant number density. This method has been used in a number of previous studies to examine galaxy formation and evolution over a large redshift range (van Dokkum et al. 2010; Papovich et al. 2011; Conselice et al. 2013; Owsnsworth et al. 2016). This has been proven to have several advantages. Although the stellar mass grows through star formation and minor mergers, the number density of galaxies above a given density threshold is invariant with time in the absence of major mergers or extreme changes of star formation (Owsnsworth et al. 2016). Selecting galaxies through this method directly tracks the progenitors and descendants of massive galaxies at all redshifts (e.g., Mundy et al. 2015; Owsnsworth et al. 2016).

We select a sample of galaxies using a constant number density of $1 \times 10^{-4} \text{ Mpc}^{-3}$, yielding a sample size of 521 galaxies.

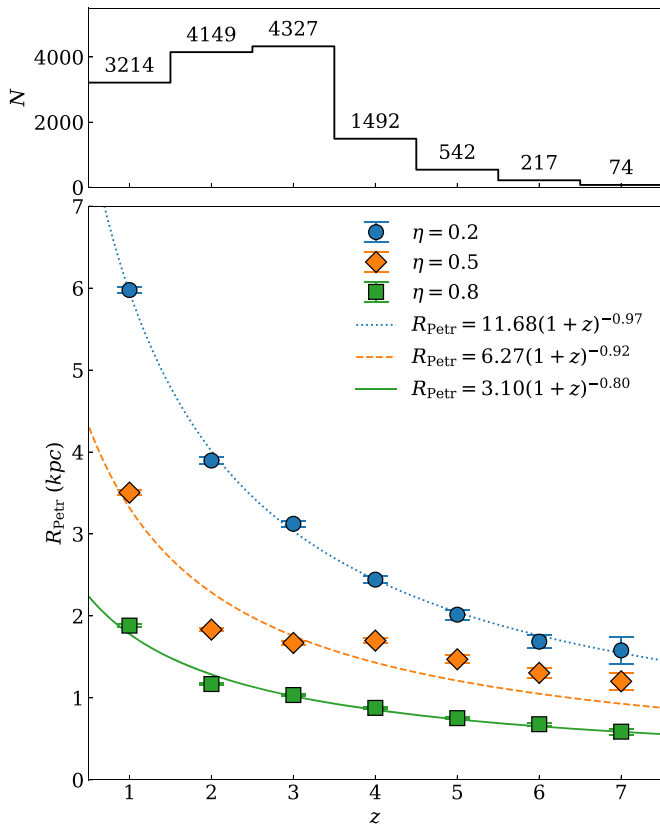


Figure 8. Top: histogram showing the distribution and number of galaxies in each redshift bin. Bottom: evolution of the average Petrosian radius through redshift for the mass-limited sample where a mass cut of $10^9 M_\odot \leq M_* \leq 10^{10.5} M_\odot$ is applied. Each point is the median value for each redshift bin, with the error bars showing the standard error. Blue circles show how $R_{\text{Petr}}(\eta = 0.2)$ changes, orange diamonds show $R_{\text{Petr}}(\eta = 0.5)$, and green squares show $R_{\text{Petr}}(\eta = 0.8)$. By fitting a power-law relation to the median sizes, we find $R_{\text{Petr}}(\eta = 0.2) = 11.68(1+z)^{-0.97 \pm 0.03}$ (blue dotted line), $R_{\text{Petr}}(\eta = 0.5) = 6.27(1+z)^{-0.92 \pm 0.03}$ (orange dashed line), and $R_{\text{Petr}}(\eta = 0.8) = 3.10(1+z)^{-0.80 \pm 0.03}$ (green solid line).

Figure 9 shows the evolution of the median corrected radii for this selected sample. As for Figure 8, the blue circles represent $R_{\text{Petr}}(\eta = 0.2)$, orange diamonds represent $R_{\text{Petr}}(\eta = 0.5)$, and green squares represent $R_{\text{Petr}}(\eta = 0.8)$. We fit a power law to the median sizes. We show these fits in Table 4 and in Figure 9 as a blue dotted line for $R_{\text{Petr}}(\eta = 0.2)$, an orange dashed line for $R_{\text{Petr}}(\eta = 0.5)$, and a green solid line for $R_{\text{Petr}}(\eta = 0.8)$. We find that $R_{\text{Petr}}(\eta = 0.2)$ changes by a factor of 3.39 ± 0.54 over the redshift range $1 < z < 7$, a much more significant change compared to a factor of 2.59 ± 0.24 for $R_{\text{Petr}}(\eta = 0.8)$ over the same redshift range.

4.6. Inner versus Outer Regions

In order to determine where the radius changes the most, we plot the normalized difference between the median $R_{\text{Petr}}(\eta = 0.2)$ and $R_{\text{Petr}}(\eta = 0.8)$ against redshift in Figure 10, where $R_{\text{Petr}}(\eta = 0.2)$ corresponds to the outer edges of a galaxy and $R_{\text{Petr}}(\eta = 0.8)$ corresponds to the inner regions of a galaxy. The normalized difference in the radii is given by

$$\Delta R_{\text{Petr}} = \frac{R_{\text{Petr}}(\eta = 0.2) - R_{\text{Petr}}(\eta = 0.8)}{R_{\text{Petr}}(\eta = 0.8)}. \quad (8)$$

The difference between the radii measured at the outer edge and the inner regions for both the mass-selected and number-

Table 4

Fits Determined for the Mass-selected and Number-density-selected Samples

η	Mass		Number Density	
	α	β	α	β
0.2	11.68 ± 0.16	-0.97 ± 0.03	12.62 ± 1.10	-0.82 ± 0.14
0.5	6.27 ± 0.10	-0.92 ± 0.03	4.57 ± 0.48	-0.53 ± 0.16
0.8	3.10 ± 0.04	-0.80 ± 0.03	2.66 ± 0.18	-0.67 ± 0.11

Note. As given by Equation (7).

density-selected samples is shown in Figure 10. The mass-selected sample is represented by the red diamonds and the number-density-selected sample by black squares. Here, ΔR_{Petr} increases as redshift decreases for both samples, but more significantly for the number-density-selected sample.

4.7. Galaxy Merger Sizes

It has long been shown that galaxies increase in size as redshift decreases (e.g., Daddi et al. 2005; Trujillo et al. 2007; Buitrago et al. 2008; Cimatti et al. 2008; van der Wel et al. 2008; van Dokkum et al. 2008; Cassata et al. 2010), but the method through which this occurs is largely unknown. We examine a sample of galaxies classified as mergers and nonmergers in order to determine whether this is a potential factor in causing the increase in size.

We identify a sample of mergers and nonmergers from the mass-selected sample by utilizing the CAS approach (Conselice 2003) whereby merging galaxies are those with a high asymmetry that is larger than the clumpiness. We use the condition

$$(A > 0.35) \text{ and } (A > S) \quad (9)$$

to define our sample. This method predominantly identifies only major mergers where the ratio of the stellar masses of the progenitors is at least 1:4 (Conselice 2003, 2006; Lotz et al. 2008).

We show the evolution of the Petrosian radii at three different η values in Figure 11. Mergers are represented by circles, and nonmergers are represented by triangles. The colors are the same as in Figure 8, where $R_{\text{Petr}}(\eta = 0.2)$ is shown in blue, $R_{\text{Petr}}(\eta = 0.5)$ is shown in orange, and $R_{\text{Petr}}(\eta = 0.8)$ is shown in green. For both mergers and nonmergers, the radius decreases as redshift increases irrespective of the value of η . However, the nonmergers are on average smaller than the mergers at the same redshift, despite having similar masses of $10^{9.5} M_\odot$ and $10^{9.4} M_\odot$, respectively. The outermost radii change the most significantly for mergers and nonmergers, changing by factors of 3.14 ± 0.49 and 4.38 ± 0.46 , respectively. The value of $R_{\text{Petr}}(\eta = 0.8)$ changes the least with mergers and nonmergers, evolving by factors of 2.62 ± 1.84 and 3.28 ± 0.18 , respectively. This is a sign that there is more evolution in the outer radii sizes for mergers than for normal galaxies. During the merger process, we see that galaxies are getting larger not in their centers but in their outer parts. This is further evidence for our observational picture that galaxies are forming from the inside out.

5. Discussion

Using the GOODS North and GOODS South fields of the CANDELS data set, we present an analysis of the sizes of a sample of galaxies in the redshift range $1 \leq z \leq 7$. We also

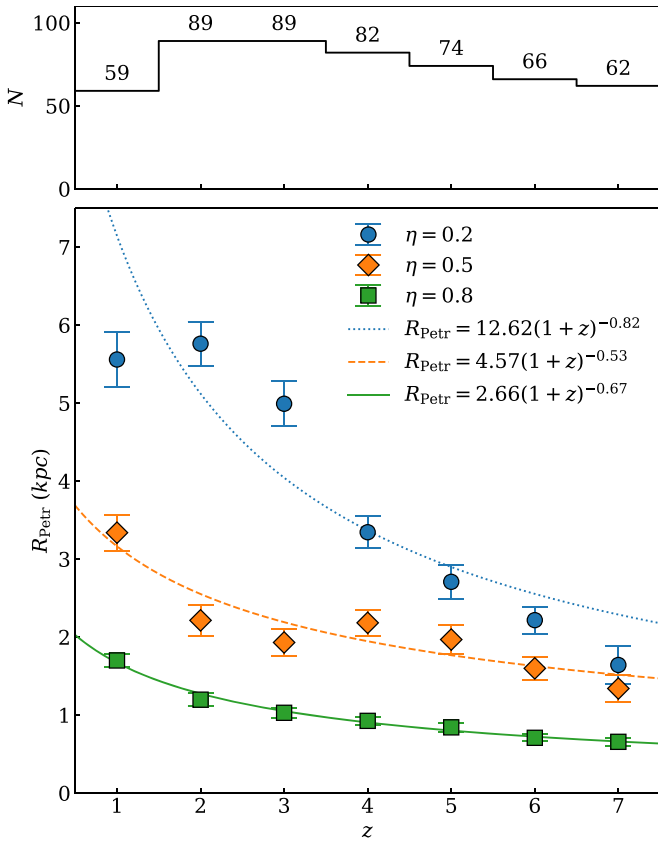


Figure 9. Top: histogram showing the distribution and number of galaxies in each redshift bin. Bottom: evolution of the average Petrosian radius through redshift for the number-density-selected sample where galaxies within a constant number density of $1 \times 10^{-4} \text{ Mpc}^{-3}$ are selected. Each point is the median value for each redshift bin, with the error bars showing the standard error. Blue circles show how $R_{\text{Petr}}(\eta = 0.2)$ changes, orange diamonds show $R_{\text{Petr}}(\eta = 0.5)$, and green squares show $R_{\text{Petr}}(\eta = 0.8)$. A power-law relation is fit to each radius, and we find $R_{\text{Petr}}(\eta = 0.2) = 12.62(1+z)^{-0.82 \pm 0.14}$ (blue dotted line), $R_{\text{Petr}}(\eta = 0.5) = 4.57(1+z)^{-0.53 \pm 0.16}$ (orange dashed line), and $R_{\text{Petr}}(\eta = 0.8) = 2.66(1+z)^{-0.67 \pm 0.11}$ (green solid line).

present a new method of removing nearby unrelated field objects from images by making use of a two-dimensional Lyman-break method at $\lambda_{\text{rest}} = 912 \text{ \AA}$. Using these processed images, we measure the redshift-independent Petrosian radius of each galaxy at η values of 0.2, 0.5, and 0.8, and determine how these radii change with redshift. The measured radii are then corrected to remove any effects from the PSF.

At high redshifts, i.e., $z > 3$, the size distribution of the galaxies within the full sample is dominated by galaxies with a small Petrosian radius, with the median size increasing as redshift decreases. This is true for all values of η . Typically, the effective radius has been used to measure the size evolution of galaxies. For example, Shibuya et al. (2015) find sizes that decrease significantly toward high z , no matter what statistic is used. In addition, a small sample of galaxies at $z \sim 9\text{--}10$ studied by Holwerda et al. (2015) were found to have mean size of $0.5 \pm 0.1 \text{ kpc}$, which is consistent with extrapolated low-redshift data.

In order to remove biases introduced by the detection limits of the surveys, we select a mass-complete sample of galaxies from the main sample within the mass range $10^9 M_{\odot} \leq M_* \leq 10^{10.5} M_{\odot}$. At $z = 7$, we find the average size of a galaxy is $R_{\text{Petr}}(\eta = 0.2) = 1.58 \pm 0.16 \text{ kpc}$, a factor of 3.78 ± 0.39

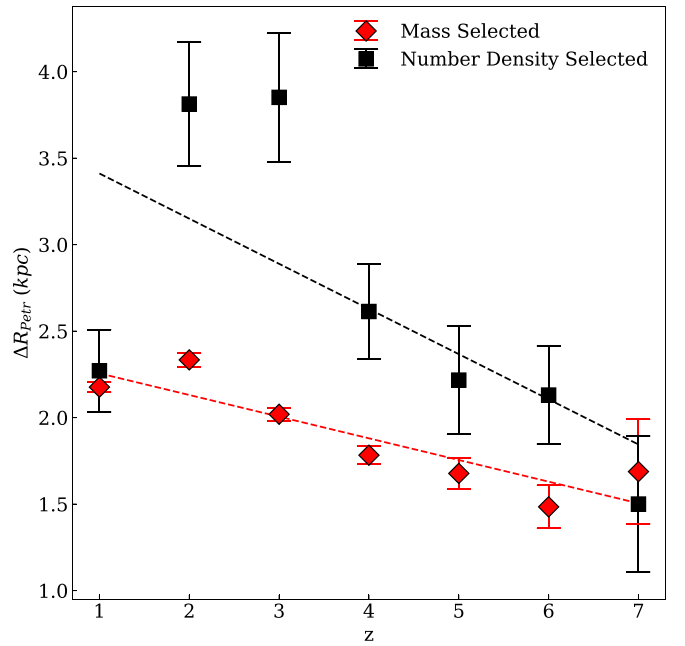


Figure 10. Evolution in the normalized median difference between $R_{\text{Petr}}(\eta = 0.2)$ and $R_{\text{Petr}}(\eta = 0.8)$ for each redshift bin. This parameter, ΔR_{Petr} , is shown in Equation (8). Mass-selected sample is shown as red diamonds and number-density-selected sample as black squares. For both samples, there is an increase in ΔR_{Petr} . Each redshift bin contains the same number of galaxies as in Figure 8 for the mass-selected sample and Figure 9 for the number-density-selected sample.

smaller than $R_{\text{Petr}}(\eta = 0.2)$ at $z = 1$. By applying a simple power-law fit to each of the radii, we see the radii change as $(1+z)^{\beta}$, where $\beta < 0$, in Figure 8. We fit $\beta = -0.97 \pm 0.03$ for $R_{\text{Petr}}(\eta = 0.2)$ and $\beta = -0.80 \pm 0.03$ for $R_{\text{Petr}}(\eta = 0.8)$, which shows that the size evolution is, on average, faster for the outer regions of the galaxies than for the inner regions. These fits are, however, shallower than other studies that use a simple fitted half-light radius. For example, Allen et al. (2017), find $\beta = -0.89$ for a mass-complete ($M_* > 10^{10} M_{\odot}$) sample of galaxies from the FourStar Galaxy Evolution Survey over a redshift range of $z = 1\text{--}7$. Similarly, van der Wel et al. (2014) determine the size evolution of a sample of galaxies with $M_* \sim 10^{10} M_{\odot}$ to be steep, with $\beta = -1.1$.

A similar result is achieved when measuring the sizes of a number-density-selected sample at a limit of $1 \times 10^{-4} \text{ Mpc}^{-3}$. The median size for this selection at $z = 7$ is $1.64 \pm 0.24 \text{ kpc}$, a number similar to that found at the same redshift for the mass-selected sample. The value at $z = 1$ for the number-density-selected sample is a factor of 3.39 ± 0.54 larger than that at $z = 7$. The size evolution for this sample therefore evolves at a rate similar to that of the previous mass-selected sample.

We again find that the evolution can be fit as a power law of the form $(1+z)^{\beta}$. For $R_{\text{Petr}}(\eta = 0.2)$, we find $\beta = -0.82 \pm 0.14$; for $R_{\text{Petr}}(\eta = 0.8)$, we find $\beta = -0.67 \pm 0.11$. The result for the outermost radius is consistent with that of Bouwens et al. (2004), who find $\beta = -1.05$, as well as with Oesch et al. (2010), who find $\beta = -1.12$ for their samples. In comparison, Patel et al. (2013) select galaxies using a number density of $1.4 \times 10^{-4} \text{ Mpc}^{-3}$ and find a value of $\beta = -1.16$ for quiescent galaxies, which is slightly higher. The results found by these previous works are determined using the effective radii of galaxies.

Independent of the selection method used, the outer radii of galaxies evolve with a slope steeper than that of the inner radii,

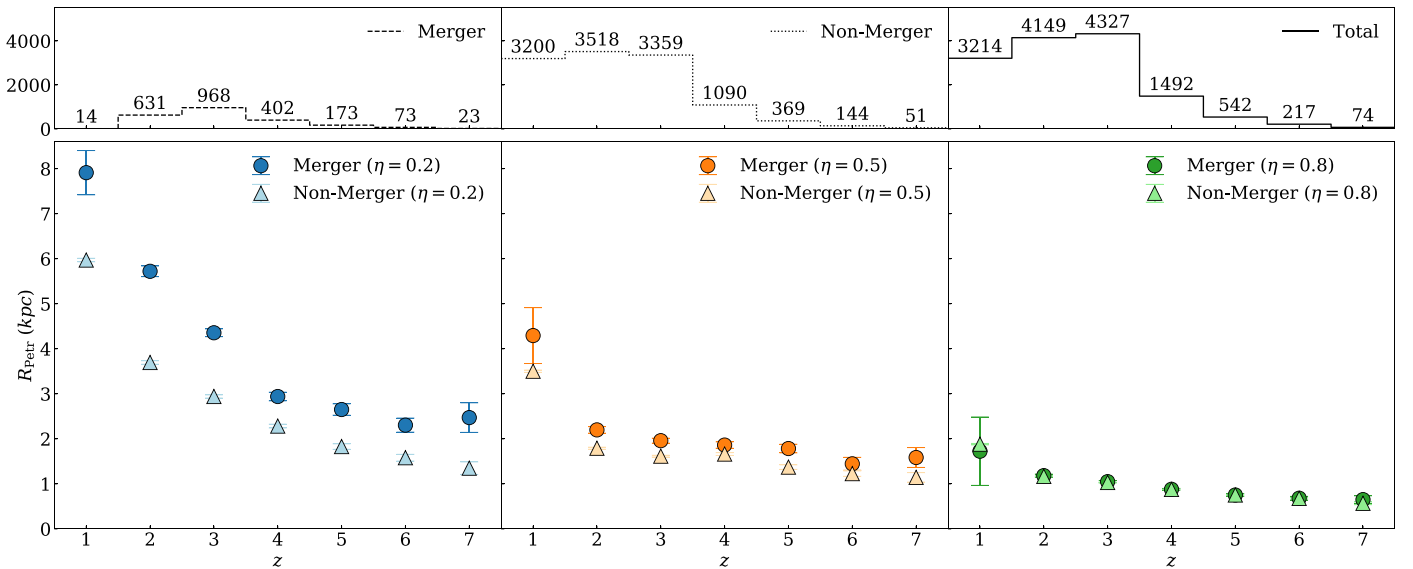


Figure 11. Top: numbers of galaxies in each redshift bin for the mergers (left), nonmergers (middle), and the total mass-selected sample (right). Bottom: evolution of the median Petrosian radius for mergers and nonmergers within the mass-selected sample. The error bars represent the standard error, some of which are smaller than the point size. Mergers are shown by circles, and nonmergers are shown by triangles. The Petrosian radius is plotted for the three different η values, with $\eta = 0.2$ shown in blue (left), $\eta = 0.5$ in orange (center), and $\eta = 0.8$ in green (right). For all redshifts, the mergers are larger on average than the nonmergers, but similar at larger η .

suggesting that the outer regions are growing more rapidly. This in turn suggests that mass is added to the outer regions in an inside-out formation mode. The difference in evolution between $R_{\text{Petr}}(\eta=0.2)$ and $R_{\text{Petr}}(\eta=0.8)$ is highlighted in Figure 10. For each selection method, the value of ΔR_{Petr} increases with time, showing that the outermost radius increases at a greater rate than the innermost radius.

We furthermore split the mass-selected sample into mergers and nonmergers, based on the measured CAS values. We examine this because the merging of galaxies is a dominant method for forming distant galaxies, and therefore we can determine how the size distribution changes during this process. Figure 11 shows that each of the different radii increase as redshift decreases for both mergers and nonmergers; however, mergers are larger on average. As with the previous samples, $R_{\text{Petr}}(\eta=0.2)$ changes the most significantly with mergers, which change by a factor of 3.11 ± 0.81 , whereas nonmergers evolve in size by a factor of 3.98 ± 0.41 . Here, $R_{\text{Petr}}(\eta=0.8)$ changes the least with mergers and nonmergers, changing by factors of 2.07 ± 0.24 and 2.31 ± 0.13 , respectively. The outer radii change to a higher degree for mergers compared to nonmergers, again suggesting an inside-out formation scenario whereby galaxy formation events increase the outer sizes more than the inner radii.

This inside-out growth could be due to a number of factors, with these results suggesting accretion of satellite galaxies to be an important one (e.g., Ferreras et al. 2014; Huertas-Company et al. 2016; Buitrago et al. 2017). Miller et al. (2019) suggest that the growth of the inner parts of galaxies is related closely to the star formation whereas the growth of the outer regions is linked to accretion and the relationship with galactic halos. By measuring r_{20} and r_{80} as opposed to the half-light radius, which is more commonly used, they find that star-forming galaxies are larger than quiescent galaxies in the inner regions (r_{20}), but the difference between the sizes of star-forming and quiescent galaxies disappears at r_{80} .

The results we find are consistent with previous work. For example, Margalef-Bentabol et al. (2016) determine the size evolution of a sample of two-component galaxies with stellar masses $M_* > 10^{10} M_\odot$ from CANDELS. They measure the circularized effective radius of each of the components and find that the outer components increase in size from $z = 3$ to $z = 1$ by a factor of 2, whereas the bulges—or inner components—remain roughly constant over the same redshift range. They conclude that this suggests inside-out formation, with the bulges being in place early on in a galaxy’s history. Carrasco et al. (2010) also find a similar result: by using observations of massive ($M_* \sim 4 \times 10^{11} M_\odot$) galaxies from the Palomar Observatory Wide-Field Infrared survey, they show that the outer regions of low- z elliptical galaxies are denser than the high- z compact massive galaxies by a factor of ~ 2 , confirming that mass is added in the outer edges. Therefore, it is now commonly seen in all studies that galaxies are growing in an inside-out fashion.

6. Conclusions

The details of the processes that lead to the growth of galaxies through time are still largely unknown, but by measuring sizes using redshift-independent relative surface-brightness metrics, we are able to determine where the size of a galaxy grows most rapidly—and therefore suggest how galaxies grow. In this paper, we present a new method of removing foreground objects from images of galaxies, making use of the Lyman break at 912 \AA . This allows us to reduce the risk of contamination from other objects when measuring the sizes and other properties of galaxies. The images we use to make our measurements are in the optical rest frame at $\lambda \cong 4000 \text{ \AA}$ wherever possible. However, due to the limited availability of *HST* bands, this is not possible for galaxies at $z > 3$, where we are forced to probe galaxy sizes in progressively bluer wavelengths down to the UV. We calculate the Petrosian radii of three different samples of galaxies selected from the CANDELS GOODS North and South

fields, and determine how these radii evolve with redshift from $z = 7$ to $z = 1$. We use the Petrosian radius as a proxy for size throughout. Overall, we find an increase in size from $z = 7$ to $z = 1$, with the outer radii increasing the most rapidly over this redshift range. This rapid growth in the outer edges suggests an inside-out formation process is causing the overall growth in galaxy size.

We also determine how size evolves for a sample of mergers and nonmergers, and find that mergers are on average larger than nonmergers at the outer radii for a given redshift. The outer radii evolve more rapidly than the inner radii, further supporting the idea that the size evolution of galaxies is caused by an inside-out formation process, e.g., the accretion of satellite galaxies, mergers, and accretion of gas from the intergalactic medium.

We thank the anonymous referee for all the very useful comments and suggestions that have lead to a greatly improved paper. This work is based on observations taken by the CANDELS Multi-Cycle Treasury Program with the NASA/ESA *HST*, which is operated by the Association of Universities for Research in Astronomy, Inc., under NASA contract NAS5-26555. We thank the CANDELS team for their heroic work making their products and data available. We acknowledge funding from the Science and Technology Facilities Council (STFC).

ORCID iDs

A. Whitney  <https://orcid.org/0000-0002-0685-6526>
 C. J. Conselice  <https://orcid.org/0000-0003-1949-7638>
 R. Bhatawdekar  <https://orcid.org/0000-0003-0883-2226>
 K. Duncan  <https://orcid.org/0000-0001-6889-8388>

References

- Allen, R. J., Kacprzak, G. G., Glazebrook, K., et al. 2017, *ApJL*, **834**, L11
 Bershad, M. A., Jangren, A., & Conselice, C. J. 2000, *AJ*, **119**, 2645
 Bertin, E., & Arnouts, S. 1996, *A&AS*, **117**, 393
 Bhatawdekar, R., Conselice, C. J., Margalef-Bentabol, B., & Duncan, K. 2019, *MNRAS*, **486**, 3805
 Bluck, A. F. L., Conselice, C. J., Buitrago, F., et al. 2012, *ApJ*, **747**, 34
 Bouwens, R. J., Illingworth, G. D., Blakeslee, J. P., Broadhurst, T. J., & Franx, M. 2004, *ApJL*, **611**, L1
 Brammer, G. B., van Dokkum, P. G., & Coppi, P. 2008, *ApJ*, **686**, 1503
 Bruce, V. A., Dunlop, J. S., Cirasuolo, M., et al. 2012, *MNRAS*, **427**, 1666
 Bruzual, G., & Charlot, S. 2003, *MNRAS*, **344**, 1000
 Buitrago, F., Trujillo, I., Conselice, C. J., et al. 2008, *ApJL*, **687**, L61
 Buitrago, F., Trujillo, I., Conselice, C. J., & Häußler, B. 2013, *MNRAS*, **428**, 1460
 Buitrago, F., Trujillo, I., Curtis-Lake, E., et al. 2017, *MNRAS*, **466**, 4888
 Carrasco, E. R., Conselice, C. J., & Trujillo, I. 2010, *MNRAS*, **405**, 2253
 Cassata, P., Giavalisco, M., Guo, Y., et al. 2010, *ApJL*, **714**, L79
 Cassata, P., Giavalisco, M., Williams, C. C., et al. 2013, *ApJ*, **775**, 106
 Cimatti, A., Cassata, P., Pozzetti, L., et al. 2008, *A&A*, **482**, 21
 Conselice, C. J. 2003, *ApJS*, **147**, 1
 Conselice, C. J. 2006, *ApJ*, **638**, 686
 Conselice, C. J., & Arnold, J. 2009, *MNRAS*, **397**, 208
 Conselice, C. J., Blackburne, J. A., & Papovich, C. 2005, *ApJ*, **620**, 564
 Conselice, C. J., Bluck, A. F. L., Buitrago, F., et al. 2011a, *MNRAS*, **413**, 80
 Conselice, C. J., Bluck, A. F. L., Ravindranath, S., et al. 2011b, *MNRAS*, **417**, 2770
 Conselice, C. J., Mortlock, A., Bluck, A. F. L., Grützbauch, R., & Duncan, K. 2013, *MNRAS*, **430**, 1051
 Curtis-Lake, E., McLure, R. J., Dunlop, J. S., et al. 2016, *MNRAS*, **457**, 440
 Daddi, E., Renzini, A., Pirzkal, N., et al. 2005, *ApJ*, **626**, 680
 Danjanov, I., McCarthy, P. J., Abraham, R. G., et al. 2009, *ApJ*, **695**, 101
 Dayal, P., & Ferrara, A. 2018, *PhR*, **780**, 1
 Duncan, K., Conselice, C. J., Mortlock, A., et al. 2014, *MNRAS*, **444**, 2960
 Duncan, K., Conselice, C. J., Mundy, C., et al. 2019, *ApJ*, **876**, 110
 Erb, D. K., Pettini, M., Shapley, A. E., et al. 2010, *ApJ*, **719**, 1168
 Fan, L., Lapi, A., De Zotti, G., & Danese, L. 2008, *ApJL*, **689**, L101
 Ferguson, H. C., Dickinson, M., Giavalisco, M., et al. 2004, *ApJL*, **600**, L107
 Ferreras, I., Lisker, T., Pasquali, A., Khochfar, S., & Kaviraj, S. 2009, *MNRAS*, **396**, 1573
 Ferreras, I., Trujillo, I., Marmol-Queralto, E., et al. 2014, *MNRAS*, **444**, 906
 Fiac, M., & Rocca-Volmerange, B. 1997, *A&A*, **326**, 950
 Furlong, M., Bower, R. G., Crain, R. A., et al. 2017, *MNRAS*, **465**, 722
 Giavalisco, M., Dickinson, M., Ferguson, H. C., et al. 2004, *ApJL*, **600**, L103
 Grogin, N. A., Kocevski, D. D., Faber, S. M., et al. 2011, *ApJS*, **197**, 35
 Henriques, B. M. B., White, S. D. M., Lemson, G., et al. 2012, *MNRAS*, **421**, 2904
 Holwerda, B. W., Bouwens, R., Oesch, P., et al. 2015, *ApJ*, **808**, 6
 Hopkins, A. M., & Beacom, J. F. 2006, *ApJ*, **651**, 142
 Huertas-Company, M., Bernardi, M., Perez-Gonzalez, P. G., et al. 2016, *MNRAS*, **462**, 4495
 Ichikawa, T., Kajisawa, M., & Akhlaghi, M. 2012, *MNRAS*, **422**, 1014
 Koekemoer, A. M., Faber, S. M., Ferguson, H. C., et al. 2011, *ApJS*, **197**, 36
 Kron, R. G. 1995, in *Evolution in the Galaxy Population*, ed. A. R. Sandage et al. (Berlin: Springer), 233
 Lani, C., Almaini, O., Hartley, W. G., et al. 2013, *MNRAS*, **435**, 207
 Law, D. R., Steidel, C. C., Erb, D. K., et al. 2007, *ApJ*, **656**, 1
 Lopez-Sanjuan, C., Le Fevre, O., Ilbert, O., et al. 2012, *A&A*, **548**, A7
 Lotz, J. M., Jonsson, P., Cox, T. J., & Primack, J. R. 2008, *MNRAS*, **391**, 1137
 Mager, V. A., Conselice, C. J., Seibert, M., et al. 2018, *ApJ*, **864**, 123
 Margalef-Bentabol, B., Conselice, C. J., Mortlock, A., et al. 2016, *MNRAS*, **461**, 2728
 McLure, R. J., Dunlop, J. S., de Ravel, L., et al. 2011, *MNRAS*, **418**, 2074
 Miller, T. B., van Dokkum, P., Mowla, L., & van der Wel, A. 2019, *ApJL*, **872**, L14
 Mundy, C. J., Conselice, C. J., & Owersworth, J. R. 2015, *MNRAS*, **450**, 3696
 Naab, T., Johansson, P. H., & Ostriker, J. P. 2009, *ApJL*, **699**, L178
 Oesch, P. A., Bouwens, R. J., Carollo, C. M., et al. 2010, *ApJL*, **709**, L21
 Ono, Y., Ouchi, M., Curtis-Lake, E., et al. 2013, *ApJ*, **777**, 155
 Ono, Y., Ouchi, M., Shimasaku, K., et al. 2010, *ApJ*, **724**, 1524
 Owersworth, J. R., Conselice, C. J., Mundy, C. J., et al. 2016, *MNRAS*, **461**, 1112
 Papovich, C., Dickinson, M., Giavalisco, M., Conselice, C. J., & Ferguson, H. C. 2005, *ApJ*, **631**, 101
 Papovich, C., Finkelstein, S. L., Ferguson, H. C., Lotz, J. M., & Giavalisco, M. 2011, *MNRAS*, **412**, 1123
 Papovich, C., Giavalisco, M., Dickinson, M., Conselice, C. J., & Ferguson, H. C. 2003, *ApJ*, **598**, 827
 Patel, S. G., van Dokkum, P. G., Franx, M., et al. 2013, *ApJ*, **766**, 15
 Petrosian, V. 1976, *ApJL*, **209**, L1
 Ribeiro, B., Le Fevre, O., Tasca, L. A. M., et al. 2016, *A&A*, **593**, A22
 Salmon, B., Papovich, C., Finkelstein, S. L., et al. 2015, *ApJ*, **799**, 183
 Schaerer, D., & de Barros, S. 2010, *A&A*, **515**, A73
 Shibuya, T., Ouchi, M., & Harikane, Y. 2015, *ApJS*, **219**, 15
 Steidel, C. C., Giavalisco, M., Pettini, M., Dickinson, M., & Adelberger, K. L. 1996, *ApJL*, **462**, L17
 Straatman, C. M. S., Labbe, I., Spitler, L. R., et al. 2015, *ApJL*, **808**, L29
 Taylor-Mager, V. A., Conselice, C. J., Windhorst, R. A., & Jansen, R. A. 2007, *ApJ*, **659**, 162
 Trujillo, I., Conselice, C. J., Bundy, K., et al. 2007, *MNRAS*, **382**, 109
 van der Wel, A., Franx, M., van Dokkum, P. G., et al. 2014, *ApJ*, **788**, 28
 van der Wel, A., Holden, B. P., Zirm, A. W., et al. 2008, *ApJ*, **688**, 48
 van Dokkum, P. G., Franx, M., Kriek, M., et al. 2008, *ApJL*, **677**, L5
 van Dokkum, P. G., Whitaker, K. E., Brammer, G., et al. 2010, *ApJ*, **709**, 1018
 Weinzirl, T., Jogee, S., Conselice, C. J., et al. 2011, *ApJ*, **743**, 87
 Wellons, S., Torrey, P., Ma, C.-P., et al. 2016, *MNRAS*, **456**, 1030
 Windhorst, R. A., Taylor, V. A., Jansen, R. A., et al. 2002, *ApJS*, **143**, 113